

# Observations of Shoaling Density Current Regime Changes in Internal Wave Interactions

AVIV SOLODOCH, JEROEN M. MOLEMAKER, AND KAUSHIK SRINIVASAN

*Department of Atmospheric and Oceanic Sciences, University of California in Los Angeles, Los Angeles, California*

MARISTELLA BERTA

*Istituto di Scienze Marine, Consiglio Nazionale delle Ricerche, La Spezia, Italy*

LOUIS MARIE

*Institut Francais de Recherche pour l'Exploitation de la Mer, Plouzané, France*

ARJUN JAGANNATHAN

*Department of Atmospheric and Oceanic Sciences, University of California in Los Angeles, Los Angeles, California*

(Manuscript received 1 August 2019, in final form 16 April 2020)

## ABSTRACT

We present in situ and remote observations of a Mississippi plume front in the Louisiana Bight. The plume propagated freely across the bight, rather than as a coastal current. The observed cross-front circulation pattern is typical of density currents, as are the small width ( $\approx 100$  m) of the plume front and the presence of surface frontal convergence. A comparison of observations with stratified density current theory is conducted. Additionally, subcritical to supercritical transitions of frontal propagation speed relative to internal gravity wave (IGW) speed are demonstrated to occur. That is in part due to IGW speed reduction with decrease in seabed depth during the frontal propagation toward the shore. Theoretical steady-state density current propagation speed is in good agreement with the observations in the critical and supercritical regimes but not in the inherently unsteady subcritical regime. The latter may be due to interaction of IGW with the front, an effect previously demonstrated only in laboratory and numerical experiments. In the critical regime, finite-amplitude IGWs form and remain locked to the front. A critical to supercritical transition eventually occurs as the ambient conditions change during frontal propagation, after which IGWs are not supported at the front. The subcritical (critical) to critical (supercritical) transition is related to Froude number ahead (under) the front, consistently with theory. Finally, we find that the front-locked IGW (critical) regime is itself dependent on significant nonlinear speed enhancement of the IGW by their growth to finite amplitude at the front.

## 1. Introduction

Salinity and temperature fronts are a common occurrence in coastal regions where rivers and other waterways outflow. The corresponding high horizontal density gradients result in a baroclinic horizontal pressure gradient force, which can strongly influence the dynamics and circulation in the shelf and beyond. Several circulation patterns of the buoyant outflow typically

emerge. The first is a geostrophic alongshore density current that is typically prograde, that is, in the direction of a Kelvin wave. The second pattern is a cyclostrophically balanced buoyant bulge with anticyclonic circulation around the outflow (Horner-Devine et al. 2015). The bulge tends not to propagate, but may repeatedly grow and break up (Yankovsky and Chapman 1997; Horner-Devine 2009). A third circulation pattern is transient density currents, with fronts of width from meters to kilometers in scale. Here we refer to free

---

Supplemental information related to this paper is available at the Journals Online website: <https://doi.org/10.1175/JPO-D-19-0176.s1>.

---

Corresponding author: Aviv Solodoch, [asolodoch@atmos.ucla.edu](mailto:asolodoch@atmos.ucla.edu)

---

*Publisher's Note:* This article was revised on 22 October 2020 to include a more specific data availability statement after the Acknowledgments, which also provides additional information about the satellite data used.

DOI: 10.1175/JPO-D-19-0176.1

© 2020 American Meteorological Society. For information regarding reuse of this content and general copyright information, consult the [AMS Copyright Policy](#) ([www.ametsoc.org/PUBSReuseLicenses](http://www.ametsoc.org/PUBSReuseLicenses)).

(rather than traveling along-coast) density currents, that is, a nonlinear flow pattern, where the horizontal pressure gradient force is balanced mainly by advection. Free density currents may form when the outflow flux variability is high enough, such as in strongly tidal conditions (Horner-Devine et al. 2009); or where density anomalies are high enough to force direct propagation even from slow, balanced, initial conditions (Sarkar et al. 2016; Warner et al. 2018; Pham and Sarkar 2018).

Density current theory is well developed and supported by decades of extensive laboratory measurements and numerical modeling (Simpson 1997; Ungarish 2009; Griffiths 1986). For times short enough compared with an inertial day (Gill 1982), the Coriolis force may be neglected. The circulation is then predominantly in the cross-frontal direction, toward the denser side at the surface, with a return flow at depth (in case of a buoyant surface anomaly rather than a deep dense anomaly). Another salient feature is then a “head wave” of elevated mixing, which forms under the surface front. Benjamin (1968) derived an analytical solution for the propagation speed of a homogeneous density current moving relative to a homogeneous ambient, depending on the density difference, layer thickness, and head loss. Benjamin’s theory was extended to allow for entrainment in a semiempirical manner by Britter and Simpson (1978), who also largely confirmed the framework in careful laboratory experiments.

Since Benjamin’s work, theoretical density current models accounting for stratified conditions (Ungarish 2006, 2009, 2012) have been developed. Stratification generally changes the propagation speeds of density currents, and additionally supports internal gravity waves (IGW). These can be excited at the front, be trapped by it, while possibly growing in amplitude and finally emitted (Nash and Moum 2005; White and Helfrich 2008; Kilcher and Nash 2010; White and Helfrich 2012). Frontal emission of IGWs can drain large fractions of density current energy (Pan and Jay 2009; White and Helfrich 2012). Finally, interactions between the IGW and density current may also slow down the latter periodically (Maxworthy et al. 2002; Goldman et al. 2014).

Several comparisons of density current observations with theory were previously conducted (Luketina and Imberger 1987; Marmorino and Trump 2000; O’Donnell 2010). These observations were within weakly stratified ambients, and compared favorably with classical (unstratified layers) density current theory. Here we present measurements taken around a propagating Mississippi

plume front<sup>1</sup> in stratified conditions within the Louisiana Bight and present a comparison with stratified density current theory.

The Mississippi outflow plume differs from most of the plume front areas studied observationally in recent years (Garvine and Monk 1974; Luketina and Imberger 1987; O’Donnell et al. 1998; Orton and Jay 2005; Horner-Devine et al. 2009; O’Donnell 2010; Kilcher and Nash 2010) on account of the combination of strong stratification, weak tides, and large discharge rate (largest annual mean discharge rate in the United States) (Walker et al. 2005). The main contribution to the study of the smaller frontal scales on the bight was made by Wright and Coleman (1971), who focused on the mixing and initial expansion at exits of the Mississippi channel. Since then, most studies of the dynamics of the Mississippi plume on the bight have concentrated on the larger scales of the plume, and the effects of wind on formation of the coastal current and outflow bulge (e.g., Rouse 1998; Walker et al. 2005; Schiller et al. 2011; Androulidakis et al. 2015). In contrast, our focus here is on characterization of the frontal circulation of a free density current in the far-field away from the outflow and (to a lesser extent) the larger-scale ambient circulation it is embedded within.

Our measurements were conducted in early May 2017 during the SPLASH campaign (<http://carthe.org/splash/>). The front was observed during two consecutive days of airplane sea surface temperature (SST) measurements and satellite imagery, and was sampled in situ repeatedly using a number of platforms and instruments during a 8-h period. The rest of the paper is structured as follows: in section 2 we present the measurements taken, auxiliary datasets, and data processing methods. The frontal propagation and surface velocity field are first described in section 3a, based mainly on drifter observations and remote sensing. In section 3b, the density structure across the front is analyzed, based mainly on a novel towed instrument array. In section 3c sections of full-depth velocity measurements are used to separately characterize the small-scale frontal circulation pattern, and a larger ambient circulation. In section 4a we conduct comparisons of the frontal propagation speed with stratified density current theory. The presence of IGW and their possible interaction with the front are examined in section 4b. A summary and discussion are given in section 5.

## 2. Data and methods

During 1–2 May 2017, in situ and remote observations were taken of a propagating salinity front in the Louisiana Bight. Two small, fast boats were used for in situ measurements and deployments of drifters, the University

---

<sup>1</sup> Plume refers in this context to the buoyant layer accumulating offshore of a river outflow.

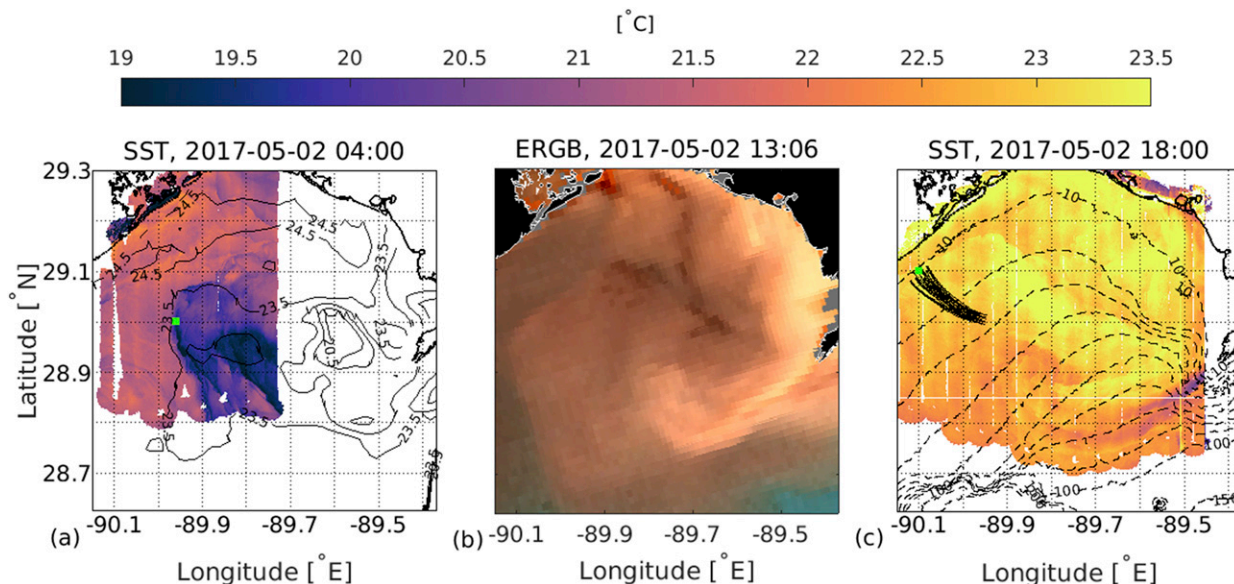


FIG. 1. Satellite and plane imagery. (a),(c) SST ( $^{\circ}\text{C}$ ; in color) imagery from the UCLA plane. Acquisition times are indicated in each title, but each panel is a mosaic of images taken over several continuous flight hours. The indicated times in (a) and (c) (0400 and 1800 CDT, respectively) correspond to the locations of the green square marker in each panel. The green square in (a) also represents the deployment position of CARTHE drifters later that day. In (a), SST contours from an earlier (0230 CDT of same day) MODIS *Aqua* overpass are superimposed. In (c), the 1200–1815 CDT trajectories of drifters deployed near the front are shown in solid black lines. Bathymetric depth is marked by dashed line in (c), between 10 and 100 m, at 10-m intervals, as well as the 150- and 200-m isobaths. The coastline is shown in a thick black line. The main outflow to the Louisiana Bight occurs at the Southwest Pass, the elongated landmass just north of the  $28.9^{\circ}\text{N}$  latitude tick mark on the east boundary of each panel. (b) Enhanced RGB image processed from VIIRS satellite 2 May 1306 CDT overpass data. ERGB color intensity (not related to color bar) is generally expected to grow with surface sediment concentration.

of California, Los Angeles (UCLA) Kodiak and the Rosenstiel School of Marine and Atmospheric Science (RSMAS) Argus. The front was located using aerial SST observations (section 2d) during the preceding nighttime (Fig. 1a). An animation (SA1) of trajectories of the vessels and drifters is accessible in the online supplemental material.

Between 1100 and 1200 central daylight time (CDT), the Argus deployed 25 Consortium for Advanced Research on Transport of Hydrocarbon in the Environment (CARTHE) drifters (section 2a) in an approximate raster pattern, at  $\approx 500\text{-m}$  intervals. Following that, the Argus took CTD casts on both sides of the front (section 2c). The Kodiak took continuous measurements along its path using several instruments. These included a towed instrument array continuously sampling the temperature and salinity down to 9-m depth while driving (section 2c) and a boat-mounted ADCP (section 2b). Since the front propagated shoreward at relatively high speed (section 3a), the general sampling strategy employed by the Kodiak was to cross the front in a given direction, drive for about 7 min, turn back, return to the front, and repeat in the opposite direction. This completed one cycle, or two sections. A total of 15 sections were taken by the Kodiak between 1130 and

1530 CDT, about 500 m away from the front to each side. The front was easily identified visually by a line (henceforth, frontal foam line) of buoyant material and foam, collocated with a peak in horizontal gradient of sea surface salinity (SSS).

Due to the advection of dynamic and tracer fields by the front, it is convenient to present data in a cofrontal coordinate system,  $(x, y)$ , where  $y$  is cross front and pointing toward the saline side, and  $x$  points alongfront  $90^{\circ}$  to the right of  $y$ . The fluid velocity components in the  $x$  and  $y$  directions are denoted by  $u$  and  $v$ , respectively. The  $x$  dependency of variables is generally suppressed, since little systematic change or variations are observed alongfront over the duration of our observations.

The orientation of the frontal coordinates is taken as constant in time and space, which is found to be a very good approximation (section 3). Therefore, knowledge of the location of a single point on the front at any given time, along with the orientation angle, is sufficient to determine the frontal line. The location of such a point is identified in one of two ways. For Kodiak-based sections, maximal SSS gradient is a natural identifier of frontal crossings due to the narrowness and amplitude of the signal. Comparison with a few records of times of foam-line crossings in the ship log corroborates this

identification method. A linear interpolation in time between two adjacent Kodiak frontal crossing positions approximately identifies the instantaneous position of a point on the front. For CARTHE drifter measurements, the needed frontal point is taken as the position of drifter 5 (i.e., the fifth deployed; see animation SA1), since it was deployed near the front and represents its velocity well (section 3a).

All data are presented in central daylight time. Many measurements are presented as composites, or means, in three different periods: 1100–1230, 1230–1330, and 1330–1500 CDT. These will be denoted by periods 1, 2, and 3, respectively. A composite is computed by binning a variable within each individual section in 5-m cross-front distance intervals. The following subsections present the specifications and methodologies for each of the main instruments used. Mean plume front positions and associated mean seabed depths at each period are given in appendix A. For context, meteorological conditions are reported in the supplemental material. The main acronyms and terms used in the paper appear in appendix F.

#### a. Surface drifters

CARTHE drifters (Novelli et al. 2017) follow the average currents over the top 50–60 cm of the ocean. The drifters are designed to minimize Stokes drift, as well as windage effects. A Spot Trace GPS unit is installed on each drifter to track its trajectory, so water velocities and other properties may be calculated. The positions are reported at approximate 5-min intervals, with  $\approx 5$ -m accuracy (Fig. 1 in Novelli et al. 2017).

Twenty-five drifters were deployed in a  $5 \times 5$  grid, with 500-m spacing in the zonal and meridional directions. Drifter numbers in the text relate to deployment positions as follows: 1 is the southwestern-most drifter, 2–5 deployed sequentially to its north, 6 the next one east of 5, 7–10 sequentially south of 6, etc.

#### b. Boat-mounted ADCP

The Kodiak was equipped with a Nortek Signature 1000 ADCP. Four of the ADCP's five beams were used, with the maximal possible acquisition rate, 16 Hz. A hydrofoil was fitted around the instrument to reduce turbulence and bubble formation in front of the transducers. The ADCP was mounted from the side of the boat, such that the transducers were at a mean depth of about 30 cm underwater. A bin size of 25 cm was used and the blanking distance was 10 cm, putting the top ADCP bin center at  $\approx 0.5$ -m depth. Maximal range (30 m) was deeper than the sea floor in the observations. The seafloor depth is detected offline as well by the vertical maximum in 4-beam-mean echo amplitude, to which a running median with 10-sample width is applied.

The bottom 15% of depth bins are removed to avoid data contaminated by sidelobe interference (Gordon 1996).

Heading corrections were applied, following a calibration, from the boat dual GPS antenna. The ADCP (GPS) data were nominally low-pass filtered using a second-order Chebyshev type-2 filter, with a cutoff period of 4 s (8 s), and 20-dB stopband attenuation relative to passband. Depth-independent signals, indicative of sudden boat movements, were additionally filtered by the following procedure. A depth averaged velocity was calculated, and a low-pass-filtered version of it calculated by applying a Loess filter of span 200 m. Then the unfiltered depth-average flow was removed (subtracted) from the total signal, and the low-pass-filtered series added to it instead. After filtering, composites for periods 1–3 were computed (section 2). Finally, the depth-average flow filtering was repeated on the composited data.

#### c. Towed instrument array

A towed instrument array (TIA) was designed to allow deployment from a small boat. Each of the array's instruments (loggers) measure temperature  $T$  and/or salinity  $S$  and/or depth (pressure  $P$  in fact). They are connected to a metal wire at regular intervals. The wire is towed behind the boat, and a “wing” supplying negative lift is connected to the bottom of the wire. The momentarily depth of a logger is determined by its pressure reading, with a typical error of 0.01 m. Depth of loggers not equipped with pressure sensors is determined by linear interpolation of depth loggers above and below them, or by extrapolation if there are no pressure loggers in one direction. Modeling and observations (A. Solodoch et al. 2020, unpublished manuscript) show that the change of line angle with depth is smooth enough to make the depth error associated with linear interpolation (extrapolation with 1-m far neighbor) of depth for the configuration used in the present observations quite small, 0.035 (0.05) m.

During the 2 May observations the TIA line was stacked with 10 loggers, at intervals of 1 m. Five of the loggers were RBR model TDR-2050, which have  $P$  (0.01 m) and  $T$  (0.002°C) sensors, and the other five were JFE model Infinity-A7CT, which have  $T$  (0.01°C) and  $S$  (0.01 psu) sensors. Numbers in parentheses denote instrumental measurement accuracy. The  $S$  sensors are in fact conductivity sensors of course, and the salinity accuracy given here takes into account the inaccuracies in temperature and conductivity together, and their influence on salinity inaccuracy for the measured range of values. These two types of loggers (TS and TP) were laid out on the line in an interleaving manner, with a TS logger on top, a TP logger second, a TS logger following it in the third position, etc.

The Kodiak is additionally fitted with an intake system, which continuously provides near-surface water to a SBE45 MicroTSG Thermosalinograph, measuring near SSS and SST to accuracy of 0.005 psu and 0.002°C, respectively. The surface sampler is treated as another TIA data point, at a depth of 0.3 m, which is an estimate of the pump intake depth. Composites of TIA data are created as described in section 2, after linear interpolation vertically between loggers.

Vertical CTD sections taken on both sides of the front, with vertical resolution as fine as 0.1 m, confirm that no persistent patterns are missed by TIA measurements due to its lower vertical resolution. That includes (section 3b) the approximate linear stratification within the shallow plume layer, as well as the relatively well-mixed or homogeneous shallow layer outside the plume.

#### d. Remote sensing

Aerial and satellite based imagery are used to determine the large-scale motion of the river plume across the bight. The plume front is recognized in the imagery by a strong SST gradient, or by color intensity gradients in the RGB and ERGB images. The latter contrast is presumably due to elevated sediment or dissolved material concentration.

Aerial SST images were taken from a Parthnavia P86 airplane equipped with an infrared imaging system during the SPLASH campaign. Multiple flight tracks, obtained while flying in a raster pattern, were combined to create composite SST maps covering areas of about 50 km × 50 km with 5-m resolution. Each raster pattern was acquired during 4–6 h of flight, and therefore the time displayed in plane-derived SST figures in this paper corresponds to one specific point chosen for a reference point of interest in each image. Further information regarding the airplane instrument package and data processing, as used in the previous LASER campaign, is given in Rasche et al. (2017) and D'Asaro et al. (2018).

Satellite red–green–blue (RGB) images and enhanced RGB images (ERGB), based on VIIRS and MODIS satellite data, were provided courtesy of the University of South Florida Optical Oceanography Laboratory (<https://optics.marine.usf.edu>). These included 2 May 2017 MODIS *Terra* 1155 CDT, VIIRS 1306 CDT, MODIS *Aqua* 1325 CDT, and VIIRS 1448 CDT overpasses.

### 3. Results

#### a. Plume propagation and surface circulation

During the nighttime before 2 May 2017 an SST front was identified in the Louisiana Bight using the airborne infrared imaging system (Fig. 1b). A coarser resolution, MODIS *Aqua* SST image from earlier that night is shown

as well. The two consistent SST patterns suggest the cold anomaly in the center and east of the bight is due to the Mississippi river discharge plume, as later confirmed in situ by its low salinity. The Mississippi outflow is often colder than the ambient water it drains into (Walker et al. 2005).

The 2 May daytime plane and satellite imagery, taken between 1155 and 1800 CDT (section 2d), show westward propagation of the front occurred between each pair of overpasses during this time. Imagery from 1306 and 1800 CDT is shown in Fig. 1. The difference between the frontal locations in temporally consecutive imagery may be used to estimate the frontal velocity component in the cross-front direction,  $0.7 \pm 0.05 \text{ m s}^{-1}$  between 1155 and 1448 CDT. In its motion, the front aligned with and coherently approached the western bight shoreline. The front appears quite straight over its >20-km length on this northwestern side, as quantified below.

The drifters were deployed either on the plume side of the front up to 4 km away from it, or no more than 100 m from it on the saline side. Their motions are representative of surface circulation (section 2a). All drifters converged toward the front in time. That may be seen from the drifters' trajectories overlaid on the remote imagery (Fig. 1), or from the animation in the supplemental material. A few drifters seen in the figure as trailing the front were in fact retrieved from the front foam line slightly earlier than the imagery time. Drifters that were not retrieved continued the shoreward propagation (not shown) and got caught in a prograde coastal current after reaching a distance of around 2 km from the coastline. These eventually beached sometime during the nighttime.

The positions, in the frontal reference frame (section 2), of the CARTHE drifters right after their deployment (1203 CDT), and again just before commencement of retrieval (1624 CDT) are shown in Fig. 2a. The figure suggests high horizontal convergence and/or strain values were sustained up to a distance of at least  $\approx 4$  km from the front. Thirteen drifters which were initially closer to the front (marked with filled symbols) converged to a (frontal) line. Indeed, these drifters were shortly after picked up from the frontal foam line (between 1630 and 1800 CDT). Based on animation SA1, the relative deformation and near convergence to a frontal line of these 13 drifters has mostly concluded before 1624 CDT.

To estimate the frontal angle on the horizontal plane, the linear least squares fit to the positions of these 13 CARTHE drifters is computed (blue line in Fig. 2a). Additionally plotted in Fig. 2a are the frontal crossings of both vessels, in the moving frontal coordinate frame (section 2). The root-mean-square deviation from the line considering both CARTHE drifters and boat

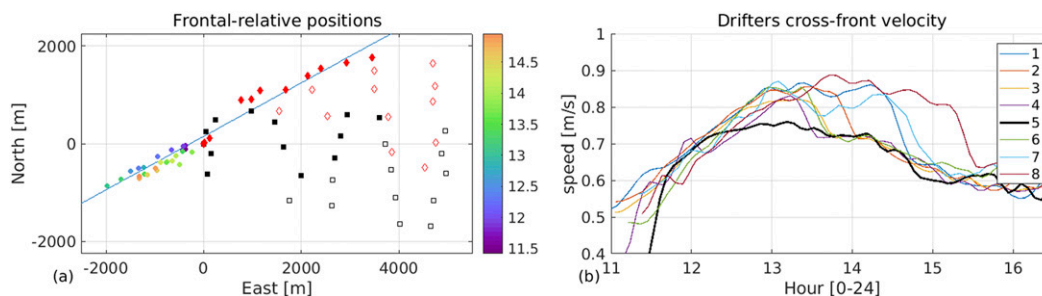


FIG. 2. (a) Position of CARTHE drifters relative to the instantaneous frontal position after deployment (black squares) at 1203 CDT, and just before retrieval began, at 1624 CDT (red diamonds). Drifters which eventually reached the front are color filled. Note that what appears like a slightly thicker red diamond at the coordinates' origin is in fact four very close solid diamonds and a solid square. Approximate frontal line (see text) shown in blue. All frontal crossings of both boats are marked in circles color-coded for frontal crossing time. The positions of all crossings were propagated to 1624 CDT (see text) with the velocity of the closest drifter. (b) Cross-front velocity of individual CARTHE drifters (drifter number given in legend). Drifter 5, which was seeded on the frontal foam line, is shown in a thick black line.

crossings is 120 m, and the median absolute deviation is 70 m, over the sampled frontal length  $\approx 6$  km. The line fit suggests a frontal orientation angle of  $28.7^\circ$  anticlockwise to east. Similar fits done on drifter positions 1 or 2 h earlier are quite similar and return angles different by up to  $5^\circ$ , although fewer drifters were on the front at these earlier hours.

Plane SST imagery (in higher magnification than displayed here) also shows that the undulations in the front are mostly smaller than 100 m in the area of deployment of the drifters. The imagery shows that the frontal orientation along its 20-km-long northwest face (detected using a maximal gradient method) is very similar to that found from the in situ measurements here. For example, in the VIIRS 1448 CDT overpass, the orientation is  $\approx 29^\circ$ . These observations support the assumption of along-frontal homogeneity. Henceforth, the frontal angle value we use in calculations is the one quoted above.

The distribution of surface velocity within the plume can be investigated through the drifter motions. The cross-front velocity component of several drifters is plotted against time in Fig. 2b. Between 1155 and 1448 CDT the cross-frontal velocity of drifter 5, which was seeded on the frontal line, is  $0.72 \pm 0.03 \text{ m s}^{-1}$ . That is similar to the velocity estimated (above) from the remote imagery over the same time window. An along-front velocity of similar or slightly smaller magnitude than the across-front component occurs as well (not shown), consistent with the clockwise turning of the drifter trajectories (Fig. 1c).

As seen in Fig. 2b, drifters experienced “sudden” (15–20 min long) cross-frontal deceleration events, in which their cross-frontal velocity reduced by  $0.1\text{--}0.2 \text{ m s}^{-1}$ .<sup>2</sup> Examination of the spatial trajectories (animation SA1, supplemental material) of individual drifters shows these decelerations occurred as the drifters converged to and aligned with the plume front. Indeed, during a deceleration event, the velocity of a drifter approaches that of drifter 5, and later remains close to it. Thus, a convergence field was established within the plume and toward the front with overtaking velocity (Britter and Simpson 1978)  $0.1\text{--}0.2 \text{ m s}^{-1}$  from the plume interior toward the plume front.

The velocity in the cross-frontal direction within the plume decreases significantly toward the beginning of the in situ observation (Fig. 2b). That is consistent with the presence of the front in the same location it was observed from two different plane and satellite imagery during the night (Fig. 1a), as well as with frontal speed estimated prior to 1100 CDT from early frontal crossings (not shown). In the rest of the manuscript we focus on the frontal circulation relative to the ambient circulation ahead of the plume rather than on the ambient circulation (and absolute plume velocity) itself and its forcing mechanism. The latter subjects need be addressed in a future study.

#### b. Frontal thermohaline structure

Figure 3 shows composites (see section 2) of SST and SSS along the cross-front axis, using measurements from the Kodiak's surface sampler and GPS. The SSS composites change by about 6 psu across the front, over a distance of about 100 m. The mean width is 70 (110) m for the center 60% (80%) of the salinity variation. Other fronts with density gradients as strong or

<sup>2</sup> Results for drifters not shown in Fig. 2b are similar. Similar decelerations did not occur in drifter alongfront velocity component.

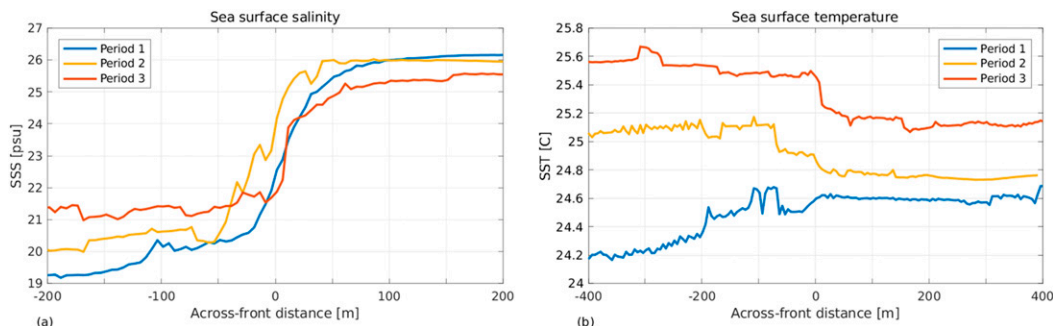


FIG. 3. Composites of (a) SSS and (b) SST vs cross-frontal distance binned at 5-m intervals. Each color represents a composite over a different period. Periods 1–3 correspond to 1100–1230, 1230–1330, and 1330–1500 CDT, respectively.

stronger were observed during SPLASH and are not unusual in this area, due to the strong influx of freshwater from the Mississippi river. Away ( $\geq 100$  m) from the front, SSS is approximately uniform in space and changes principally in time. The horizontal difference of SSS across the front decays during the course of the day from 8 to  $\sim 4$  psu. In terms of effect on density, the salinity variations are dominant, causing a density change of approximately  $5 \text{ kg m}^{-3}$  across the front, while temperature variations cause a smaller density change of order  $0.1 \text{ kg m}^{-3}$  across the front.

SST increases with time faster on the fresh side. It is colder (warmer) than the salty side early (late) in the day. That is consistent with the plane SST data (section 3a). The effect is likely due to a reduction in vertical mixing at the base of the plume (aka barrier layer) due to higher stratification, relative to the ambient. For a related discussion of barrier layer effects in freshwater plumes, see Mahadevan et al. (2016).

In Fig. 4 we present TIA composites for periods 1–3 (section 2c). The cross-front density structure is

reminiscent of a density current, especially during periods 1–2. On the plume side, a buoyant surface layer terminates abruptly at a depth of  $\approx 2$  m; its density is clearly distinguished from that of the fluid across the narrow ( $\approx 100$  m width) front. At the front, isopycnals plunge in a structure visually reminiscent of a density current head wave (Simpson 1997), in which enhanced mixing and entrainment occur. We will show in section 4 that this plunging of the isopycnals is associated with internal wave excitation or trapping at the front.

Unlike many previous observations and modeling studies, the plume occurs in a strongly stratified environment. The fluid is stably stratified, and similarly so on both sides of the front beneath  $\approx 3$ -m depth. The buoyant plume is itself also stratified, and limited to the top  $\approx 2$  m. The mean vertical density (salinity) difference is about  $4 \text{ kg m}^{-3}$  (5.5 psu) at the observed depth range on the saline side, a similar magnitude to the horizontal difference across the front at the surface. The maximal vertical temperature difference grows from  $0.7^\circ\text{C}$  in early sections to  $1.7^\circ\text{C}$  later in the day, causing a density

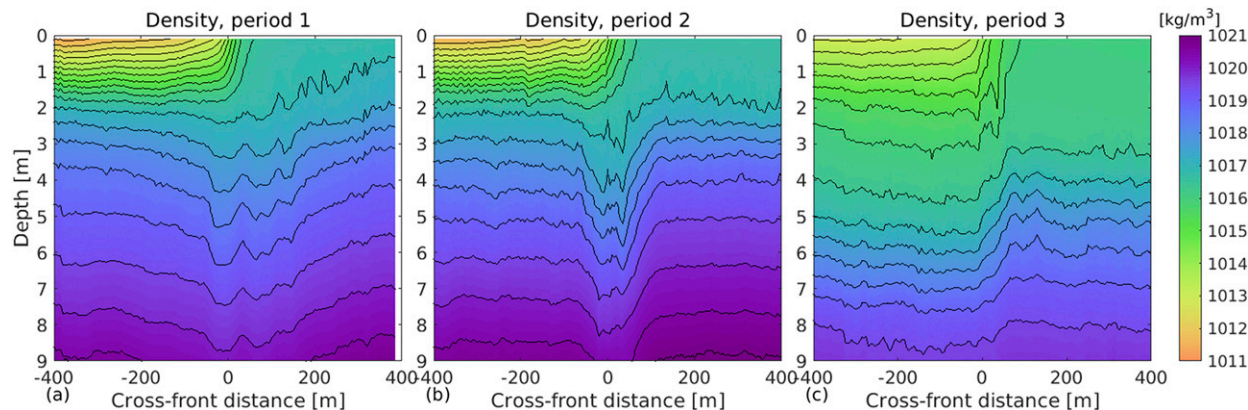


FIG. 4. TIA density data vs depth and cross-frontal distance (in 5-m-wide bins). (a)–(c) Composites for sections from periods 1–3 (1100–1230, 1230–1330, and 1330–1500 CDT, respectively) are shown. Contour interval =  $0.5 \text{ kg m}^2$ .

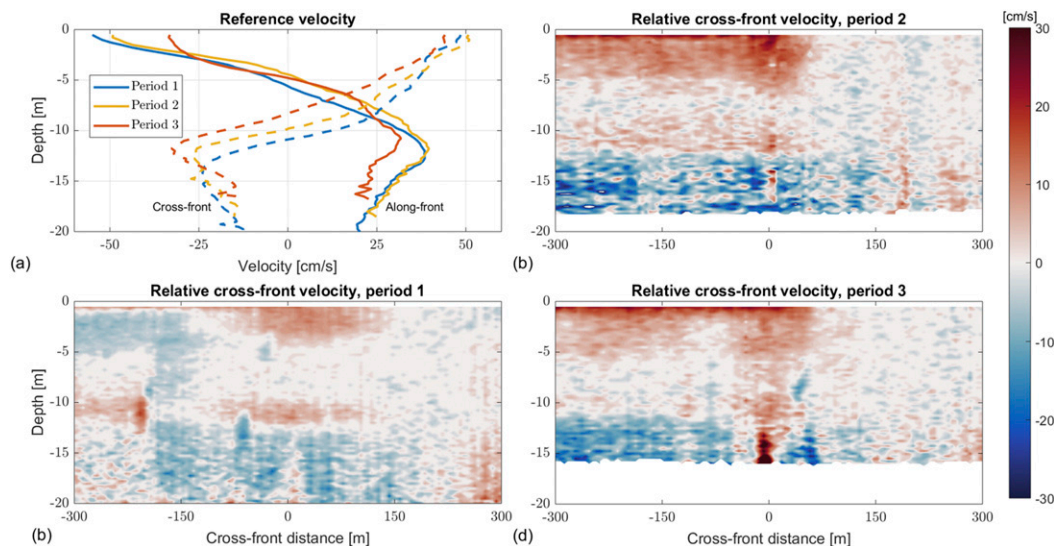


FIG. 5. Composites of velocity derived from repeated sampling sections by boat mounted ADCP, for periods 1–3 (1100–1230, 1230–1330, and 1330–1500 CDT, respectively). (a) For each period, the “reference velocity” (average velocity on the saline side, see text) vs depth is shown in frontal coordinates, e.g., cross-front and alongfront velocity components. (b)–(d) The relative (defined relative to the reference velocity) cross-frontal velocity component vs depth and cross-front distance for each period. Positive cross-front velocity values ( $y$  direction) indicate velocities toward the saline side. Positive alongfront velocity values indicate velocities  $90^\circ$  to the right of  $y$ .

difference of only  $\approx 0.5 \text{ kg m}^{-3}$ . Thus, temperature is negligible relative to salinity in determining the density variations at depth as well.

A gradual freshening of the layer immediately beneath the original plume occurs over time, possibly due to vertical mixing. A more dramatic evolution occurred in period 3 as the entire observed water column freshens up. Due to the strong vertical shear of velocity (section 3c), material at depth originates farther west relative to material at the surface. The freshening at depth may thus be the result of a previous freshening of the western bight area, which could have occurred via a bottom-attached prograde coastal current [section 1 here and Yankovsky and Chapman (1997)] fed by Mississippi outflows. Consistently, unretrieved drifters were eventually entrained within a prograde coastal current (section 3a).

### c. Frontal velocity structure

Horizontal velocity data were obtained from the boat-mounted ADCP (section 2). A second downward-looking ADCP was attached to a drifting buoy and deployed on the frontal foam line at 1330 CDT; comparison was conducted with the boat-mounted ADCP measurements in the vicinity ( $\pm 50 \text{ m}$ ) of the front. The instruments show excellent agreement in pattern and amplitude of the velocity profile considering they were not collocated. Therefore, velocity data are presented based on the boat-mounted ADCP measurements alone.

The surface velocity from drifters (section 3a) showed velocity approximately homogeneous up to 4 km away from the front on the plume side. Therefore we decompose the depth-dependent flow field  $\underline{u}$  as the sum of a reference velocity  $\underline{U} = (U, V)$  independent of horizontal position, and a relative velocity  $\underline{u}' = (u', v')$ , that is,  $\underline{u}(y, z, t) = \underline{U}(z, t) + \underline{u}'(y, z, t)$ . The reference velocity field is defined at each depth as the average of the measured velocity on the saline side between a distance of 100–500 m from the front. As discussed before, we assume along-frontal homogeneity. The usefulness of the decomposition is clearly seen in Fig. 5: 1) the magnitude of the reference velocity  $\underline{U}$  is significantly larger than the  $\underline{u}'$  magnitude in most areas, and 2) the relative velocity displays a clear frontal structure in its cross-front component  $v'$ , that is, variation over a short distance across the front, as further discussed below. Therefore, the introduced decomposition may be understood effectively as a decomposition to a frontal-scale circulation component  $\underline{u}'$  and a larger-scale circulation component  $\underline{U}$ .

The  $\underline{U}$  magnitude and direction near the surface are similar to the velocity of the deployed drifters (section 3a). The reference cross-frontal velocity is toward (away from) the saline side in the upper (lower)  $\approx 10 \text{ m}$ . A significant  $O(0.5) \text{ m s}^{-1}$  alongfront reference velocity component exists. Given the observed density field, a direct evaluation of the thermal wind equation (Gill 1982),

$$\frac{\partial u}{\partial z} = \frac{g}{f\rho} \frac{\partial \rho}{\partial y}, \quad (1)$$

predicts at the plume depths (0–2 m) an alongfront jet with vertical shear  $\partial u/\partial z \approx 7 \text{ s}^{-1}$ . Beneath the plume the result is  $\approx 0.35 \text{ s}^{-1}$ , where we disregarded the head wave and estimated  $\partial \rho/\partial y \approx \Delta \rho/\Delta y$ , with  $\Delta \rho$  based on density differences >100 m away from the front on either side, and  $\Delta y$  corresponding to the frontal thermohaline width ( $\approx 100 \text{ m}$ ). In contrast, the measured alongfront reference velocity shear values are much lower,  $\sim 0.1 \text{ s}^{-1}$  in the entire water column, and of the opposite sign to that required by thermal wind.<sup>3</sup> Thus, the frontal circulation pattern is far from geostrophic balance. We note that the alongfront reference velocity is approximately prograde at the surface (since the front aligned with isobaths), and thus may be related to presence of a prograde coastal current. The latter often occurs due to river outflow (section 1). Other evidence consistent with the presence of a prograde coastal current was mentioned in section 3b.

Composites of the relative cross-frontal velocity  $v'(y, z)$  are shown in Fig. 5 up to a distance of 300 m from the front.<sup>4</sup> The relative velocity is toward the saline side at the surface, and toward the fresh side at depth. The two-layer structure qualitatively resembles the canonical density current structure (Benjamin 1968; Simpson 1997; Ungarish 2009). A head wave like feature also appears. That is typical of gravity current fronts (section 1), although here internal waves contribute to it as well (section 4). The middepth flow is more noisy, or displays more scales of variability, but since density measurements beneath 10-m depth are unavailable, we do not comment on it further. Alongfront velocity  $u'$  (not shown) is generally less coherent than  $v'$ , and several times smaller in magnitude than  $U$ .

Since buoyant material accumulates at the surface, and since horizontal thermohaline gradients are maximal there, the frontal propagation velocity relative to the ambient (reference) flow  $v_{f,\text{obs}}$  is defined as the cross-frontal component of the relative velocity  $v'$  in the upper bin. Another, semi-independent calculation of  $v_{f,\text{obs}}$  is provided by the difference between cross-frontal velocity of drifters on the front, and the cross-frontal component of the ADCP-derived reference velocity  $V$ . The two methods give very similar results: in periods 1, 2, and 3, respectively, the drifter-based (ADCP-based) relative frontal velocities are  $v_{f,\text{obs}} = 0.08$  (0.13), 0.24

(0.22), and 0.25 (0.23)  $\text{m s}^{-1}$ . More details are given in appendix B. Thus, the relative frontal velocity grows in time, that is, the density current initially accelerates.

Cross-front convergence was observed in the motions of the CARTE drifters (section 3a). A quantitative measure of convergence is now obtained. As individual drifters converged to the front, their velocities dropped by  $\sim 0.15 \text{ m s}^{-1}$  within  $\approx 20 \text{ min}$ . Thus, the convergence distance in frontal coordinates is  $\sim 0.5 \times 0.15 \text{ m s}^{-1} \times 20 \text{ min} \approx 100 \text{ m}$ , and the convergence value is  $\approx 0.15 \text{ m s}^{-1}/100 \text{ m} \approx 40 f$ . The magnitude is confirmed in a calculation of the strain tensor from relative motions of drifter groups (Molinari and Kirwan 1975), which we shall not expand upon here. The cross-front convergence is characteristic of density currents. The convergence magnitude  $\delta$  is very high relative to mesoscale [ $\geq 10\text{-km}$  scales,  $\delta \sim O(f)$ ] ocean motions. Similar magnitudes [ $\delta \sim O(10f)$ ] were previously measured in fronts of similar or slightly larger scales (Rasche et al. 2017; D'Asaro et al. 2018) where intense submesoscale circulations (McWilliams 2016) occur. Similar and larger values ( $>100f$ ) were measured for even narrower or strongly tidal buoyant plumes (O'Donnell et al. 1998; Orton and Jay 2005).

#### 4. Comparison with stratified density current theory

The frontal-scale circulation pattern and density field diagnosed in previous sections, are qualitatively consistent with buoyant density current structure. The main points of similarity are as follows:

- 1) A sharp ( $\approx 100 \text{ m}$  wide) front separates waters of very different densities near the surface (Fig. 4). The frontal width is much lower than the Rossby radius of deformation  $R_d = NH_e/f$ , which we estimate at 5–20 km. Here  $N$  is the Brunt–Väisälä frequency, and  $H_e$  is the “equivalent depth” (Gill 1982). The value assigned to the latter is varied between the plume thickness to the full fluid depth.
- 2) Propagation of the buoyant layer into the dense “ambient,” with a return flow at depth (Figs. 5b–d).
- 3) A head wave exists at the front (Fig. 4).
- 4) A convergence occurs toward the front at the buoyant layer (sections 3a and 3c).
- 5) Consistently, the frontal circulation is far from geostrophic balance (section 3c).

Given the qualitative consistency of the frontal circulation with density current features, in this section we make a quantitative comparison of the diagnosed frontal propagation speed (section 3c) to the theoretical prediction based on stratified density current theory. In section 4a, steady stratified density current theory is

<sup>3</sup> The shear of  $u'$  composites in the upper 5 m is, like the  $U$  shear, of the opposite sign to that required by thermal wind.

<sup>4</sup> Individual sections reaching distances up to 500 m from the front do not show significant deviations from the composites shown here.

used, whereas in [section 4b](#), interactions of the density current with internal gravity waves are considered.

### a. Steady flow theory

The speed of propagation of a steady one-dimensional density current ([Ungarish 2009](#)) is approximately proportional to  $\sqrt{\Delta P/\rho}$ , where  $\Delta P$  is the hydrostatic pressure difference between both sides of the front at the plume base (lower boundary). For the case of a homogeneous density current of thickness  $h$ , propagating within a homogeneous (unstratified) ambient with total depth  $H$ , the exact relation was derived by [Benjamin \(1968\)](#), taking into account energy dissipation (but not entrainment):

$$v_f = F_B(h/H) \sqrt{\frac{\Delta P}{\rho_0}}, \quad (2)$$

$$F_B(a) = \left[ \frac{(2-a)(1-a)}{1+a} \right]^{0.5}. \quad (3)$$

The nondimensional function  $F_B$  derived by [Benjamin \(1968\)](#) is a decreasing function of  $a = h/H$ , with  $O(1)$  values.<sup>5</sup> For a thin plume ( $h/H \ll 1$ ), and if the density current and ambient are each unstratified,  $F_B$  is approximately the ratio of the frontal propagation speed to the interfacial wave speed. However, it should not be confused with the ambient Froude number defined in the next subsection. The quantity  $\rho_0$  is a reference (say, column average) density value.

Equation (2) is written here in terms of  $\Delta P$  rather than in terms of a density anomaly, although the latter form is the common formulation in the unstratified case. The present form generalizes well to stratified conditions, where Eqs. (2) and (3) still serve as an approximation to  $v_f$ , in good agreement with laboratory and numerical experiments ([Ungarish and Huppert 2002](#); [White and Helfrich 2008](#); [Goldman et al. 2014](#)). The approximation also compared well with rigorous theory developed for the limiting cases of an unstratified density current propagating within a stratified ambient ([Ungarish 2006](#)), and of a stratified density current propagating within an unstratified ambient ([Ungarish 2012](#)).

Density currents in qualitatively similar stratification conditions to the present, that is, strong stratification within the plume, mixed conditions at the same depths outside of the plume, and intermediate stratification beneath, were observed by [Warner et al. \(2018\)](#) in the equatorial Pacific. Their computations of theoretical density current speed is thus a good basis for comparison

with the stratified theory used here. We note that [Warner et al. \(2018\)](#) diagnose rather than compute  $F_B$  in their observations. The second factor in Eq. (2) is replaced in their calculations by  $\sqrt{g'h}$ , where the density difference in the reduced gravity  $g'$  is averaged over the buoyant layer depth. That is numerically very similar in these stratification conditions to our  $\sqrt{\Delta P/\rho}$  prescription, with  $\Delta P$  evaluated at the base of the plume. [Warner et al. \(2018\)](#) diagnose  $F_B \approx 0.7$ , from the ratio of observed propagation speed to  $\sqrt{g'h}$ . We note that this  $F_B$  value is the only one which can correspond to vanishing dissipation in the front ([Benjamin 1968](#)), and that a similar  $F_B$  value was also suggested to hold in density current observations in the same area by [Johnson \(1996\)](#). Thus, we suggest that previous measurements ([Johnson 1996](#); [Warner et al. 2018](#)) are plausibly consistent with the presented formulation, which follows from stratified density current theory.

The theoretical frontal speed  $v_f$  [evaluated from Eq. (2), see [appendix C](#)] and the observed frontal velocity  $v_{f,obs}$  ([section 3c](#) and [appendix B](#)) are compared in [Fig. 7](#). We find that  $v_{f,obs}$  was initially substantially lower than  $v_f$ , but grew in magnitude during period 1, attaining values within 25% of (mean deviation 10% from)  $v_f$  during each of periods 2–3. We shall see in [section 4b](#) that reasonable agreement with steady theory may be expected a priori only in periods 2–3, since at these times internal waves cannot overrun the front.

A decrease in  $v_f$  over time is predicted, and attributed (see [appendix C](#)) mainly to thermohaline changes ([section 3b](#)) and the associated decrease in the frontal pressure head. From late period 3 on, the decrease in  $v_{f,obs}$  is more rapid than the decrease in  $v_f$ . However, some extrapolation (e.g., for reference velocity) is used in deriving frontal velocities after 1500 CDT ([appendixes B and C](#)), and hence their respective errors are uncertain at that time.

The steady-state theory used in this subsection is formally invalid when IGW occur, and specifically when they overrun the front. During early period 1 the front appeared to have been almost stationary, that is, a speed decrease as one looks back in time to  $\approx 0.1$  (a third of  $v_f$ ) toward 1100 CDT. A possible reason for this early time discrepancy is suggested to be interaction with IGW, as discussed and analyzed in [section 4b](#).

### b. Density current–IGW interactions

In stratified conditions ambient IGW become possible, and stratified density current theory also deals with the interactions between the density current and the IGW in the ambient. IGWs are observed in TIA sections by the plunging of isopycnals in the vicinity of the front ([Fig. 6](#)). Isopycnals from the base of the plume to at least as deep as 9 m, plunge an extra 1–2 m at the front. In this section we

<sup>5</sup> Steady solutions exist for  $a \leq 0.5$ .

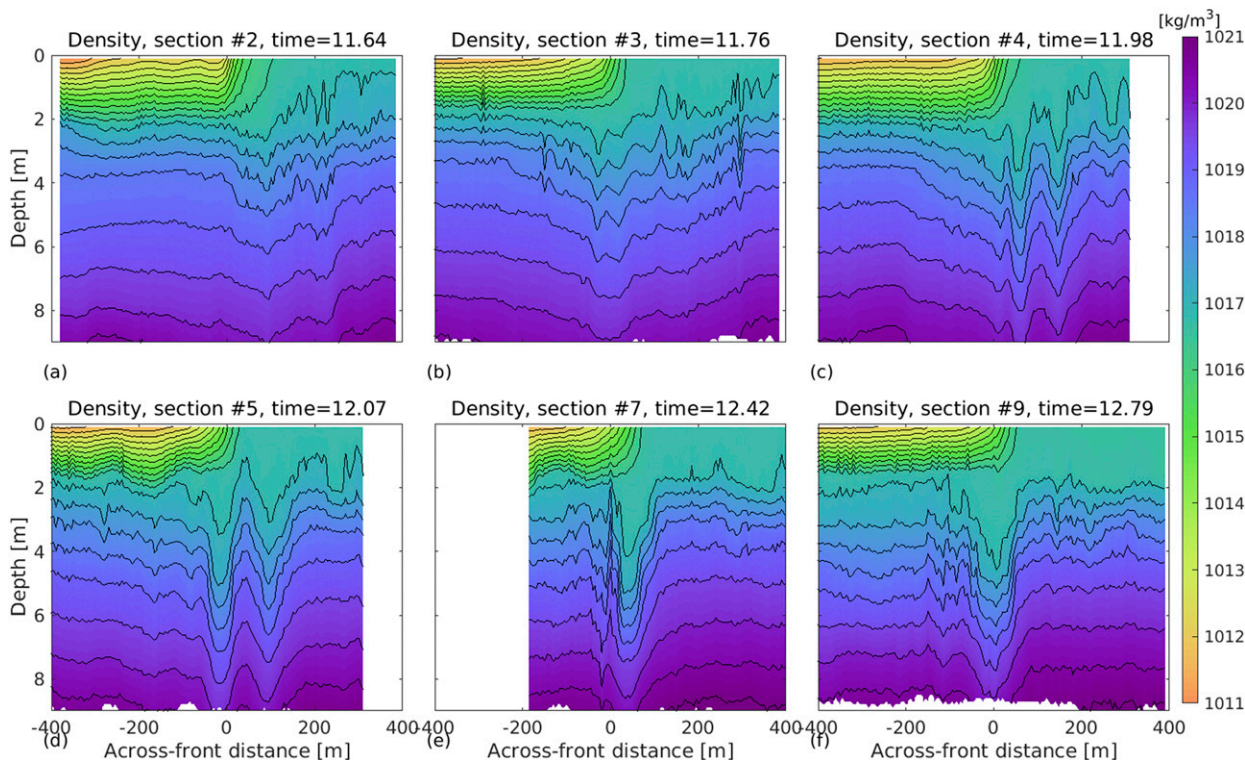


FIG. 6. TIA sections data: density vs depth and (5-m binned) cross-front distance. Each panel shows a single section with progressively later crossing time. The time given in the title for each section relates to the time of day (0–24 h) in which the front was crossed. Contour interval =  $0.5 \text{ kg m}^{-3}$ .

demonstrate and analyze several regime changes in interactions of IGW with the density current front.

### 1) SUPERCRITICAL TRANSITIONS

A key parameter in current–wave interaction is the ambient Froude number  $F_a$  (not to be confused with  $F_B$ ), here the ratio of the frontal propagation speed  $v_f$  to the fastest long-IGW speed in the ambient ahead of the density current  $c_a$ . The  $F_a$  values define the subcritical ( $F_a < 1$ ), critical ( $F_a = 1$ ), and supercritical ( $F_a > 1$ ) regimes. We also define the fastest IGW speed in the ambient under the plume  $c_u$  and the Froude number in the same region  $F_u$ .

Laboratory experiments and numerical simulations of density currents in ambient stratification (Maxworthy et al. 2002; White and Helfrich 2008) show that for  $F_a < 1$ , IGW can form at the front and overrun it, propagating to the ambient ahead of it. In the subcritical regime, waves crossing the frontal area compromise the validity of steady-state model, such as that used in the previous subsection. In contrast, IGWs may grow to finite amplitudes and remain locked to the front if the regime is critical or somewhat supercritical (Maxworthy et al. 2002; White and Helfrich 2008), that is,  $F_a \geq 1$  (a more distinguished criterion is addressed below). Finally, in

the strongly supercritical regime (at still larger  $F_a > 1$  values), no significant waves lock to the front, or propagate ahead of it, although they may appear at or propagate toward its rear.

In observations of the Columbia river plume, Nash and Moum (2005) have demonstrated a supercritical to critical  $F_a$  transition. At the initial stages of the Columbia plume life, the  $F_a$  regime was slightly supercritical, and large-amplitude IGW formed at the front. Nash and Moum (2005) suggest that the frontal convergence field converts density current kinetic energy to potential energy, which is subsequently trapped at the front as a front-locked IGW due to the supercritical condition. As the plume decelerates in its expansion and dissipation, a subcritical transition occurs, and IGW start radiating ahead of the front.

In the present observations, we find (Fig. 6) that the opposite  $F_a$  transition occurs, relative to the process observed by Nash and Moum (2005). In TIA sections during period 1, small-amplitude isopycnal disturbances are found on both sides of the front, suggesting that the regime is subcritical, that is, IGW occur that are faster than the front. However, in later TIA sections (late period 1 onward), prominent IGW are found only at the front itself, and their amplitude is

increased relative to the earlier sections. That suggests that the  $F_a$  has transitioned to a critical or supercritical value between periods 1 and 2. An additional (qualitative) condition for formation of large-amplitude front-locked IGW in the simulations of White and Helfrich (2008), that the fluid be nonlinearly stratified, is also met in our observations as the ambient stratification decreases significantly with depth, for example, a factor of  $\approx 2$  between 3- and 6-m depth (Fig. 6).

To examine the critical transition in more detail, we compute the speed of long IGW on the ambient side at each period. We take both ambient stratification and ambient velocity shear into account and obtain the IGW speeds by solving numerically the Taylor–Goldstein equation (TGE), as detailed in appendix D.

The fastest downstream IGW speeds per period  $c_a$  are displayed in Fig. 7, along with  $v_f$  and  $v_{f,obs}$ . The TGE IGW speed is seen to be higher (lower) than the instantaneous frontal speed  $v_{f,obs}$  before (after) 1200 CDT. This supports the interpretation (above) that a critical to supercritical transition occurred during the later part of period 1. Note that the sub or super critical character of the density current is insensitive to the error estimates (crosses), which are on the order of  $0.03 \text{ m s}^{-1}$ . Furthermore, a  $c_a$  estimate is produced for the beginning of period 1 (1100 CDT) as well (appendix C). Its value suggests that  $F_a$  was subcritical at early period 1 with regards to the theoretical (rather than instantaneous) frontal velocity  $v_f$  as well.

In simple stratification scenarios,  $c_a$  grows with  $H$ . For example,  $c_a = NH/\pi$  for a case of constant  $N \sim \sqrt{(\Delta\rho)_{tb}}/H$  and with a rigid lid. If the vertical top to bottom density difference  $(\Delta\rho)_{tb}$  is constant, then  $c_a \sim \sqrt{H}$ . This relation scales well for our TGE IGW solutions as well (appendix D and Fig. C1). This suggests that transition from subcritical to critical  $F_a$  occurs due to  $c_a$  reduction (and  $F_a$  increase) over time as a result of density current shoaling.

Having established the critical transition during period 1, we turn to further conditions on the formation of front-locked IGW, observed in period 2. White and Helfrich (2008) showed that a more accurate condition to their formation is (rather than  $F_a \approx 1$ )  $F_u \approx 1$  (e.g., their Figs. 13–14). The condition that the linear IGW speed under the plume be close to critical, may be roughly interpreted as allowing the copropagation with or accumulation of IGW disturbances at the front. Therefore we compute  $c_u$  as well, by solving the TGE again (appendix E). We also compute the first-order nonlinear correction to  $c_u$ . The nonlinear IGW speed,

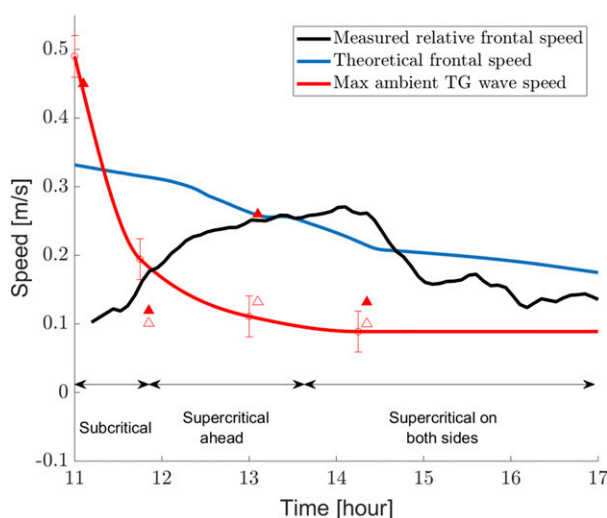


FIG. 7. The plot compares the measured  $v_{f,obs}$  (black) and steady-state theoretical  $v_f$  (blue) frontal velocities, and demonstrates that several regime transitions (approximately indicated by bottom arrows) occur in relation to IGW front speed criticality. IGW speed ahead of the plume  $c_a$  is shown in red circles at 1100 CDT, and per period 1–3 (1100–1230, 1230–1330, 1330–1500 CDT, respectively). Crosses denote  $c_a$  uncertainty estimates. The red curve is obtained by spline interpolation from the red circles, and by uniform forward extrapolation after 1500 CDT. Solid (hollow) triangles denote nonlinear (linear) IGW speed in the ambient under the plume,  $c_{nl}$  ( $c_u$ ). Triangles symbols relate to the same times as circles but are horizontally offset for visual clarity. Further details on calculations are given in section 4 and in appendixes B–D. Error estimates for  $c_u$  and  $c_{nl}$  are given in Table E1. The annotations “subcritical,” “supercritical ahead,” and “supercritical on both sides,” refer to  $F_a < 1$ , ( $F_a > 1$  while  $F_u \leq 1$ ), and both  $> 1$ , respectively.

related to the KdV equation (see appendix E), is denoted by  $c_{nl}$ .

The results for  $c_u$  and  $c_{nl}$  are shown in Fig. 7 and given in Table E1 as well. During early period 1,  $c_u$  and  $c_{nl}$  are similar<sup>6</sup> to  $c_a$ , that is, higher than  $v_f$  (subcritical regimes). However, during period 2  $c_{nl}$  is similar in magnitude to  $v_f$ , while both linear wave speeds are  $\approx 50\%$  lower. Therefore, finite-amplitude front-locked IGW developed in “tight” critical conditions in terms of the nonlinear wave speed  $c_{nl}$ . Hence nonlinearity is a decisive factor in allowing the frontal locking of IGW in period 2, and hence perhaps in attaining their larger amplitudes as well.

Unlike in period 2, at period 3  $c_{nl}$  is considerably lower than  $v_f$  (even though a nonlinear wave amplitude similar to that observed in period 2 was assumed in the period 3 calculation). That is also consistent with the disappearance of the prominent front-locked IGW in period 3 (Fig. 4c). Instead, isopycnals ahead of the plume monotonically plunge under it (compare with, e.g., White and Helfrich 2008, Figs. 11c and 12c). The front-

<sup>6</sup>The  $c_u$  and  $c_{nl}$  calculation scatter is quite low (high) for early period 1 and periods 2–3 (late period 1), as detailed in appendix E. Hence, we avoid overinterpreting late period 1  $c_u$  and  $c_{nl}$  values.

locked IGW of period 2 is presumably left behind as  $F_u$  grows in period 3, or is dissipated, but in any case cannot be supported at the front. Thus, another criticality regime transition occurs between periods 2 and 3, specifically,  $F_u$  passes from near-criticality (period 2) to supercriticality (period 3).

The changes in  $c_{nl}$  (and therefore in  $F_u$ ) over time are consistent with the presence or absence of IGWs at the front, as described above. These  $c_{nl}$  differences are in turn determined by changes in depth, ambient stratification, and ambient velocity (appendixes D and E). It does not appear straightforward to determine which of these factors have more weight in influencing the  $c_{nl}$  changes, but note that significant ambient stratification changes occur between periods 2 and 3 as the front approaches the shoreline (see discussion at end of section 3b, as well as Figs. 4 and E1).

Calculated spatial IGW properties are also consistent with the observed. The calculated period 2 plume-side<sup>7</sup> IGW isopycnal displacement  $\eta(z)$  (appendix E) peaks at depths of 3.5–4 m, in rough agreement with the observed depth of peak isopycnal plunging (Fig. 6). The horizontal scale (say, half a wavelength) of the observed IGWs (Fig. 6) is  $\approx 20$ –100 m. The specific wavelengths excited at the front were postulated by White and Helfrich (2008) to be related to the mechanism of resonant forcing over “topography,” where the latter is represented by the density current shape. While the IGW speeds displayed in Fig. 7 correspond to wavelength  $\rightarrow \infty$ , the wave speed changes very little for disturbances long compared to the fluid depth. Indeed, repeating the TGE calculations for a wavelength of 50 m changes the  $c_a$  and  $c_u$  wave speeds by only a few centimeters per second. Hence there may be said to be a supercritical transition with respect to wavelengths comparable to the observed IGWs, consistently with the observations. The calculated KdV soliton widths  $W$  (for  $c_{nl}$ , appendix E) during period 2, 40–50 m, are also similar in magnitude to the observed IGW widths in period 2.

## 2) DENSITY CURRENT DECELERATION BY IGWS

Experiments in stratified conditions show that density current interface becomes wavy in subcritical  $F_a$  conditions. In some cases, interaction with the internal wave field may cause deceleration of the gravity current in this regime. The effect was first demonstrated by Maxworthy et al. (2002), in their laboratory and numerical experiments. In their experiments the deceleration occurs when IGW troughs became aligned with the front after

propagating past it. Alignment of IGW crests with the front accelerated the latter, but to a lesser degree than the acceleration by the troughs, causing a net mean deceleration. Goldman et al. (2014) also find similar relative deceleration in numerical experiments for a stratified density current in a stratified ambient. In numerical and laboratory experiments (Maxworthy et al. 2002; Ungarish and Huppert 2006; Goldman et al. 2014), the deceleration generally occurs under the conditions that 1) the front is subcritical with respect to IGW propagation speeds and 2) the ambient vertical density difference is comparable in size to the total vertical density difference in the plume side of the front. The magnitude of the deceleration is often larger than 50%, and can also be large enough to effectively arrest the density current temporarily.

The summarized conditions for deceleration are examined in regards to our observations: 1) Fig. 7 suggests that around 1120 CDT, a subcritical to supercritical transition has occurred relative to  $v_f$ ; 2) the ambient vertical density difference is of similar magnitude (larger than 50%) relative to the total vertical difference on the plume side; and 3) the reduction in speed in period 1 relative to that predicted or observed in periods 2–3 is similar to the magnitude of deceleration in experiments (referenced above) due to IGW–front interactions. The conclusion is that it is plausible that prior to  $\approx 1130$  CDT, the density current speed was much reduced due to interaction with IGWs in a subcritical  $F_a$  condition. Once the IGW speed decreased [due to propagation of the front to shallower water, section 3b(1) and appendix D], a subcritical to supercritical transition occurred relative to  $v_f$ , which allowed  $v_{f,obs}$  to recover and gradually grow again to values close to  $v_f$ .

## 5. Summary and discussion

Detailed observations of a propagating Mississippi outflow plume and its sharp front were taken in the Gulf of Mexico’s Louisiana Bight during early May 2017. While previous observations of the Mississippi plume focused mainly on bight scale surface circulation, we focus on frontal circulation and its interaction with internal gravity waves (IGW). In the observations, the plume moved across the center of the bight, rather than as a coastal current. Thus, the large-scale spatiotemporal circulation pattern on the bight was in contrast to the archetypical patterns of semisteady circulation following river outflows, the coastal current and the recirculating bulge.

The remote sensing and the in situ data show that the front extended over 20 km in length, while its width was  $O(100)$  m, considerably smaller than the Rossby radius of deformation. It is found meaningful to decompose the

<sup>7</sup>That is, associated with  $c_u$  and  $c_{nl}$ .

flow field near the front into two components: reference (larger scale), and relative (frontal) flow fields. The relative velocity and density fields display several qualitative similarities with density currents, including a narrow front, flow away from the buoyant layer, a return flow beneath it, and a strong surface convergence within the buoyant layer toward the front. Both the plume and the ambient fluid underneath and ahead of it were strongly stratified, that is, had internal differences in density comparable to the plume–ambient difference.

The frontal circulation is therefore compared with stratified density current theory (section 4a). Previous comparisons (Luketina and Imberger 1987; Marmorino and Trump 2000; O'Donnell 2010) have used classical homogeneous density current theory, for weakly or partially stratified conditions. The observed frontal propagation speed is shown to differ by  $\approx 10\%$  on average from the stratified theory prediction during middle to late in situ observations (periods 2–3, defined in section 2). Earlier, however, the front was significantly slower, in apparent contradiction to the (steady-state) theory.

The frontal speed anomaly relative to the steady-state theory during period 1 is to be expected if conditions were in fact not steady. Indeed, repeated density sections across the front show IGW anomalies on both frontal sides during early to midperiod 1. The velocity of ambient IGWs is estimated from the TGE, which confirms that the  $F_a$  (Froude number relative to IGWs ahead of the plume) is  $< 1$  (subcritical) during that time, that is, IGWs (which may be generated at the front, e.g., Nash and Moum 2005; White and Helfrich 2008) are faster than the front, and overrun it.

Previous laboratory experiments and numerical simulations (Maxworthy et al. 2002; White and Helfrich 2008; Goldman et al. 2014) have demonstrated that a stratified density current in a subcritical regime may be slowed down significantly by interactions with the generated IGWs. Conditions at which such deceleration by IGW interactions occurred in experiments are reviewed, and appear consistent with conditions in our observations. It is therefore plausible that the slow anomaly during period 1 occurred due to interactions with IGWs in a subcritical  $F_a$  regime, a phenomenon previously demonstrated in numerical and laboratory experiments only.

The TGE calculations suggest that IGW speed at the front decreased during the observations due to the propagation of the front to shallower water. The IGW speed decrease facilitated a subcritical to critical transition by late period 1. The transition is in contrast to previous observations (Nash and Moum 2005; Kilcher and Nash 2010). In the observations of Nash and Moum (2005), large-amplitude IGW grew and remained locked to the front in the (initial) supercritical regime and radiated ahead of the front as it slowed down and transitioned to a subcritical regime.

In our observations, finite amplitude front-locked IGW appeared as  $F_a$  grew to supercritical values in period 2. Based on numerical simulations and theory, White and Helfrich (2008, 2012) show that the regime in which front-locked IGWs appear is better described in terms of criticality of  $F_u$ , the Froude number relative to linear IGW speed under the plume (rather than ahead of it,  $F_a$ ). In our observations  $F_u \approx 2$  during period 2, where the linear IGW speed is again evaluated from the TGE. Indeed, in the calculations of White and Helfrich (2008) as well, in some cases front-locked waves appeared even for  $F_u > 1$  (their Figs. 13–14). Therefore we additionally calculate the first nonlinear (KdV) correction to the internal wave speed  $c_{nl}$ . It is found that the mean  $c_{nl}$  value during period 2 is within a few percent of the observed frontal speed. That is, during the presence of finite amplitude front-locked IGWs, a “tight” criticality occurs in terms of the nonlinear wave speed. It is thus suggested that the finite-amplitude IGW criticality is enforced by the nonlinear speed enhancement, and a positive feedback may be at work.

Finally, a transition to strict  $F_u$  supercriticality occurs between periods 2 and 3, after which front-locked waves do not appear, as the front can overrun any ambient IGW. The IGW speed calculations suggest this occurs again (as in the period 1 transition) due to ambient IGW slowdown. However, in the period 3 case, it is not as clear that shoaling is (directly) a significant cause of the IGW slowdown. Rather, significant ambient stratification changes, as well as ambient shear changes, may be the main causes.

In this paper we concentrated on the dynamics of the frontal circulation, identified as a density current, and its possible interactions with internal gravity waves. We note that the reference surface velocity contributes a larger fraction of the plume velocity than the relative (frontal) velocity. Hence the large-scale (reference) velocity holds an important role in the cross-bight plume propagation, which contrasts with the more common observations of coastally trapped density currents. Further investigation of the associated large-scale cross-bight propagation pattern and its dynamical causes are thus desirable as well.

We note that a complicating factor in the presented theoretical analysis is that the front is embedded in vertically sheared ambient flow, more intense than the density current circulation. The theory and previous simulation results compared with in section 4 take ambient stratification into account. Ambient shear is taken into account as well in the IGW calculations, but not in the steady-state density current calculations conducted here. A possible alleviating factor is that the plume is limited to the top two meters of the water column, and the ambient (reference) velocity varies by a small fraction ( $\leq 10\%$ ) over the same depth.

*Acknowledgments.* This research was made possible by a grant from the Gulf of Mexico Research Initiative to the Consortium for Advanced Research on the Transport of Hydrocarbons in the Environment (CARTHE). SST data from the MODIS mission were obtained from the NASA EOSDIS Physical Oceanography Distributed Active Archive Center (PO.DAAC) at the Jet Propulsion Laboratory, Pasadena, CA (<http://dx.doi.org/10.5067/GHGMR-4FJ01>). Red–green–blue (RGB) images, and enhanced RGB images (ERGB), based on VIIRS and MODIS data, were provided courtesy of University of South Florida Optical Oceanography Lab (<https://optics.marine.usf.edu>).

*Data availability statement.* Data used in this article are publicly available through the Gulf of Mexico Research Initiative Information & Data Cooperative (GRIIDC) website: <https://data.gulfresearchinitiative.org/> under the following DOIs: [10.7266/n7-t3g4-fc07](https://doi.org/10.7266/n7-t3g4-fc07) (plane SST imagery), [10.7266/n7-wa5p-jk51](https://doi.org/10.7266/n7-wa5p-jk51) (ADCP data), [10.7266/n7-hr34-dg23](https://doi.org/10.7266/n7-hr34-dg23) (Kodiak surface sampler), [10.7266/n7-me53-7y55](https://doi.org/10.7266/n7-me53-7y55) (Towed Instrument Array), [10.7266/n7-wgt0-kw56](https://doi.org/10.7266/n7-wgt0-kw56) (CARTHE drifters), and [10.7266/QXFRAZKS](https://doi.org/10.7266/QXFRAZKS) (satellite data).

## APPENDIX A

### Mean Frontal Position per Period

The average mean position of the plume front at each of periods 1–3 (section 2) is given in Table A1. The positions are based on the mean Kodiak positions during each period (the Kodiak took repeated sections across the front). They are thus representative of the position in the cross-front coordinate (sections 2 and 3a), whereas the front by definition is elongated in the alongfront direction. The seabed depths given correspond to the given mean locations, and are approximately representative of the entire front since the front aligned with the isobaths (section 3a).

## APPENDIX B

### Observed Frontal Velocity

The observed relative frontal velocity  $v_{f,obs}$  is estimated in each period using two different methods. Both methods rely on the same reference velocity, that is, the ADCP reference cross-front velocity  $V$ , and define the relative frontal velocity as the absolute velocity measured in the front vicinity minus this reference velocity. We use the top bin of  $V$  (hereafter  $V_s$ ) in each period, since the reference cross-front velocity varies little in the top  $\approx 1$  m (Fig. 5a). The first method uses for the absolute frontal velocity the ADCP-derived absolute velocity within the top bin averaged from 50 m from the front on the fresh side to 25 m from the front on the saline side (the results are not sensitive to changes by a factor of 2 in these distance values). The second method uses the

TABLE A1. Mean frontal position and seabed depth in each averaging period (section 2).

Time	Longitude	Latitude	Seabed depth (m)
1100–1230 CDT	89.9954°W	29.0074°N	23.8
1230–1330 CDT	90.0349°W	29.0177°N	20.7
1330–1500 CDT	90.0736°W	29.0369°N	16.6

velocity of drifter 5 to define the absolute frontal velocity. Drifter 5 was present on the front at all times and is representative of velocity of other drifters on the front (section 3a). The two methods give very similar results, as detailed in Table B1.

In addition to  $V_s$  so defined at each midperiod (1145, 1230, 1415 CDT), we define  $V_s = 0.1 \text{ m s}^{-1}$  at 1100 CDT. That is in rough agreement with extrapolation of drifter 5 velocity (Fig. 2b) backward in time, as well as with (not shown) additional data based on Kodiak frontal crossings around 1045 CDT. See also discussion at end of section 3a.

To derive an “instantaneous”  $v_{f,obs}$  (used in section 4) rather than a period-averaged one, we again use the (instantaneous, this time) velocity of drifter 5 relative to the top bin ADCP measured reference velocity  $V_s$ . The period-averaged  $V_s$  values are spline-interpolated to the drifter time base. After 1500 CDT, ADCP observations were not made, and hence the reference velocity at that time (up to 1700 CDT) is defined as equal to its value at 1500 CDT. The result is smoothed with a first-order Savitzky–Golay filter with a 0.5-h window size.

## APPENDIX C

### Theoretical Frontal Velocity

To evaluate  $v_f$  from Eq. (2), we calculate  $\Delta P$  and  $h$  by values 300 m away from the front on either side, in each TIA section. The results (Fig. 7) are not sensitive to the specific distance chosen. The plume thickness  $h$  was defined based on the depth of the deepest isopycnal that surfaces on the ambient side (see Fig. 4), about 2 (2.65) m during periods 1–2 (3). The cross-front pressure difference  $\Delta P$  is calculated at depth  $h$ . It is analogous to the prescription of  $\Delta P$  at the base of dense (as opposed to buoyant) density currents in stratified ambients (Ungarish and Huppert 2002; Ungarish 2006, 2012).

A smoothed  $v_f$  is obtained by the application of a first-order Savitzky–Golay filter with a 1-h window size. The smoothed version is then extrapolated in time by assuming that the stratification profile did not differ after the last TIA section, and using bathymetric depth  $H$  of the front at each hour based on drifter positions.

To gauge the influence of reduction in  $\Delta P$  (due to thermohaline changes) over time on the frontal velocity,

TABLE B1. Relative frontal velocity  $v_{f,obs}$  estimates. Each row relates to a different averaging period 1–3 (1100–1230, 1230–1330, and 1330–1500 CDT, respectively). The “drifter-based” estimates rely on absolute velocity of drifter 5. The ADCP-based estimates rely on absolute velocity from the ship-mounted ADCP, either from its top bin, or from linearly extrapolating its measurements (0.5 m upward) to the surface based on the two top bins. All three methods rely on the ADCP-based reference velocity, which appears to vary little vertically in its top bins.

Time	Drifter based ( $\text{m s}^{-1}$ )	ADCP based (top bin; $\text{m s}^{-1}$ )	ADCP based (interpolated; $\text{m s}^{-1}$ )
1100–1230 CDT	0.08	0.13	0.16
1230–1330 CDT	0.24	0.22	0.275
1330–1500 CDT	0.25	0.23	0.3

the calculation of theoretical frontal velocity is repeated as described above, except that the factor  $\Delta P$  is kept constant at the value measured in the first section. The result, in comparison with the full calculation (Fig. C1, and compare with  $v_{f,obs}$  in Fig. 7), suggests that frontal deceleration between periods 2–3 occurred principally due to thermohaline changes.

#### APPENDIX D

##### Internal Wave Speed Calculation in Ambient ahead of Plume

The discretized Taylor–Goldstein equation (TGE) is solved using the generalized eigenvalue solver described in Jagannathan et al. (2017), with boundary conditions of no-normal flow at the top and bottom. For each observational period (section 2), the phase speeds of the fastest downstream IGW is determined, equal to the maximal real TGE eigenvalue. For the midperiod time of each period 1–3, the background vertical profiles of cross-frontal velocity and stratification considered are as shown in Figs. 5 and 4, respectively.

Uncertainty ( $\pm 0.03 \text{ m s}^{-1}$ ) was quantified first by varying the depth and strength of the peak stratification in the top 10 m, by 10% about the measured values and recomputing the IGW speeds. Second, since stratification measurements under 10-m depth were not available the reported phase speeds were calculated assuming stratification is constant beneath 9-m depth. However, we find that the deep stratification has very small impact on the maximal phase speed: changing the stratification under 10 m by  $\pm 50\%$  changes the peak phase speed by up to  $0.02 \text{ m s}^{-1}$  in the variations we attempted.

A solution for 1100 CDT was calculated as well. Since the plume was almost stationary at that time (appendix B), the density stratification was taken as identical to period 1 (1100–1230 CDT) as density changed little during period 1. The same uncertainty quantification as reported above was applied. Similarly, the reference speed was taken as identical to period 1 in vertical pattern but with amplitude multiplied by  $a = 0.2$ ,

consistently with the estimate of surface velocity at 1100 CDT (appendix B). Changes of the factor  $a$  from  $a = 0$  to  $a = 0.4$ , changed the IGW speed within the uncertainty values reported in Table E1 ( $\approx 0.1 \text{ m s}^{-1}$ ), not affecting the interpretation in section 3b. Scaling IGW speed relative to seabed depth (next paragraph, Fig. C1) also predicts similar values at 1100 CDT.

The  $c_a$  results per period are given in Table E1. The values and their cubic-spline interpolation in time are shown in Fig. 7. The smoothed curve is also extrapolated for display purposes uniformly forward in time from 1500 to 1700 CDT. To gauge the influence of depth change on the IGW speeds, we plot the TGE speed together with the quantity  $c(t) \equiv c_0 \sqrt{H(t)/H_0}$  in Fig. C1. Here  $c_0$  and  $H_0$  are the full TGE IGW speed estimate

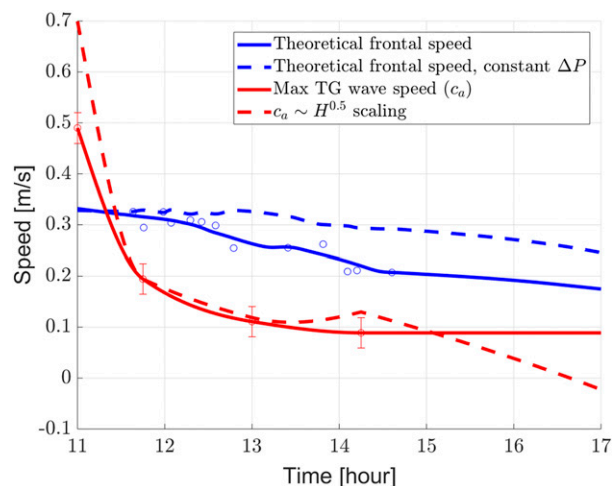


FIG. C1. Theoretical Benjamin (1968) frontal speed  $v_f$  (blue solid line) is compared with the theoretical speed where the pressure head  $\Delta P$  is kept at its initial value (blue dashed line). Estimated maximal wave speeds based on the TGE (red solid line) are compared with a scaling estimate  $c(t) = c_0 \sqrt{H(t)/H_0}$ , where  $c_0$  and  $H_0$  are the full TGE estimate and depth at 1325 CDT, and  $H(t)$  is the depth at each time. Blue circles denote  $v_f$  values calculated from density structure obtained in individual frontal crossings. The blue curve is obtained by interpolation of the blue circles data points (after 1500 CDT some quantities used in the calculation are extrapolated). Other symbols are as defined in Fig. 7.

TABLE E1. Internal gravity wave speeds (relative to reference velocity, [appendixes D and E](#)) in ambient ahead of the plume ( $c_a$ ) and under the plume ( $c_u, c_{nl}$ ). The first two are obtained via the TGE ([appendixes D and E](#));  $c_{nl}$  is the first nonlinear correction to  $c_u$  ([appendix E](#)). Mean values for each variable are given at 1100 CDT and for each period 1–3.

Time (CDT)	$c_a$ (m s <sup>-1</sup> )	$c_u$ (m s <sup>-1</sup> )	$c_{nl}$ (m s <sup>-1</sup> )
1100	0.49 ± 0.05	0.45 ± 0.1	0.45 ± 0.1
1100–1230	0.19 ± 0.03	0.10 ± 0.04	0.12 ± 0.05
1230–1330	0.11 ± 0.03	0.13 ± 0.003	0.26 ± 0.01
1330–1500	0.09 ± 0.03	0.1 ± 0.002	0.13 ± 0.003

and depth at 1300 CDT, and  $H(t)$  is the depth at each time. In simple cases of a set top to bottom density difference, uniform stratification, and no ambient velocity shear, this scaling is exact [[section 3b\(1\)](#)].

### APPENDIX E

#### Internal Waves of Finite Amplitude in Ambient under the Plume

To investigate the formation of front-locked finite-amplitude IGW in period 2 we calculate the ambient IGW wave speed under the plume. We denote by  $c_u$  the fastest such IGW at a given period. The theory and simulations of [White and Helfrich \(2008\)](#) suggest that to a good approximation, a calculation of  $c_u$  can be performed under the assumption that the plume bottom serves as a rigid lid to IGW propagating under it (see also [Ungarish 2006](#)). We solve the TGE ([appendix C](#)) using the period-averaged ambient density and velocity field under the plume, for each period.

We additionally calculate the first nonlinear correction to the TGE linear wave speed, still taking ambient shear and stratification into effect, using the methodology described by [Maslowe and Redekopp \(1980\)](#). Perturbation analysis shows that any TGE mode may occur as a horizontally compact disturbance (a soliton), governed by a Korteweg–de Vries (KdV) equation. The soliton width  $\Delta$  and its speed of propagation  $c_{nl}$  are then determined by simple integrals (which we perform numerically) of the particular TGE eigenfunction.

The functional form of the KdV soliton ([Ostrovsky and Stepanyants 1989](#)) is  $\eta = \eta_0 \text{sech}^2[(y - ct)/\Delta]$ . The width parameter  $\Delta$  is therefore approximately the half-width at half-height. For simplicity we define  $W = 4\Delta$ , which is approximately the width of the soliton at  $\eta = 0.07\eta_0$ , and to observational accuracy may be taken as the full width of the finite-amplitude disturbance that can be distinguished visually from other (smaller) undulations. We calculate  $W \approx 40\text{--}50$  m during period 2. Comparison to observed IGW widths is discussed in [section 4b](#).

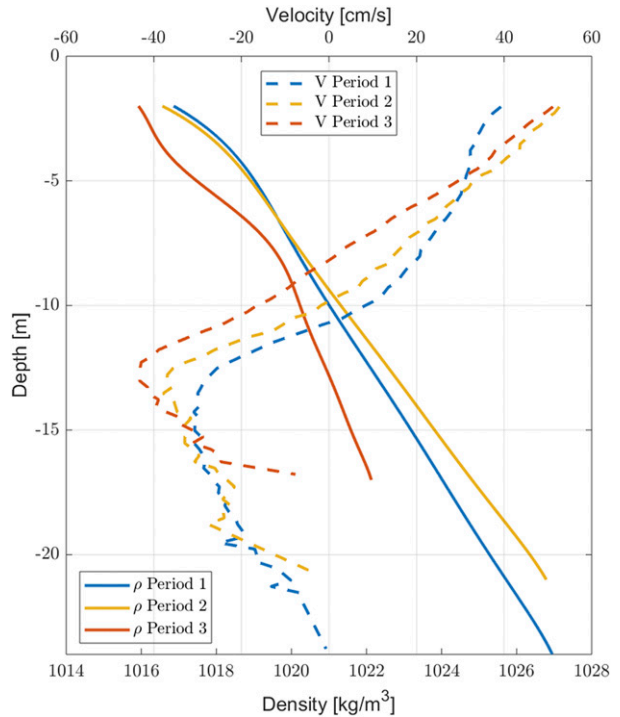


FIG. E1. Ambient density  $\rho$  and cross-front velocity  $v$  under the plume are shown in solid and dashed lines, respectively. Profiles are shown for periods 1–3 (1100–1230, 1230–1330, and 1330–1500 CDT, respectively). These are the nominal (see text for description of variations) profiles used in the  $c_u$  and  $c_{nl}$  calculations. Similar profiles for the  $c_a$  calculations (ahead of the plume, [appendix D](#)) are given in [Fig. 5](#) for  $V$  explicitly or can be deduced for  $\rho$  from [Fig. 4](#).

The asymptotic analysis used in deriving the KdV equation assumes the parameters  $\varepsilon = \eta_0/(H/\pi)$  and  $\delta = (H/\pi)^2/L^2$  to be “small” ( $\ll 1$ ), where  $L$  is a typical IGW horizontal scale, and  $H$  is the total water depth ([Lee and Beardsley 1974](#)). In our case we estimate  $\varepsilon = 0.3$  and  $\delta = 0.1$ , where we assumed  $L = \Delta$ , as computed in our period 2 solutions. Although  $\varepsilon$  is not strictly  $\ll 1$ , KdV is often reasonably accurate outside of its formal validity limits ([Ostrovsky and Stepanyants 1989](#)). Although higher-order approximations exist ([Ostrovsky and Stepanyants 1989](#); [Helfrich and Melville 2006](#)), we consider that multiple complicating factors do not justify going beyond the first nonlinear correction of  $c_u$ . Specifically, the ambient density, velocity, and depth are not constant in time (although changing slowly relative to the hypothetical soliton time scales, e.g.,  $\Delta/c$ ). Additionally, the stratification is unknown under 9 m. The latter caveat is dealt with, as in [appendix D](#), by testing various downward continuations of the observed stratification, continuously increasing or decreasing in magnitude by up to 50%. The results during periods 2–3 are highly insensitive to these variations ([Table E1](#)). The nominal (i.e., stratification

TABLE F1. Summary of acronyms, terms, and symbols commonly used in the text. At the end of each row, the section number is given where the term is defined.

Acronym	Expansion and notes
$y$	Cross-front coordinate axis, pointing toward the saline side (section 2).
$x$	Alongfront coordinate axis, pointing 90° to the right of $y$ (section 2)
Periods 1, 2, 3	1100–1230, 1230–1330, 1330–1500 CDT (section 2)
TIA	Towed instruments array (section 2c)
$v$	Velocity component in the $y$ direction (section 2)
$u$	Velocity component in the $x$ direction (section 2)
$V$	Reference velocity component in the $y$ direction (section 3c)
$U$	Reference velocity component in the $x$ direction (section 3c)
$v'$	Relative velocity component in the $y$ direction (section 3c)
$u'$	Relative velocity component in the $x$ direction (section 3c)
$v_f$	Theoretical steady-state frontal propagation speed (section 4a and appendix C)
$v_{f,obs}$	Observed frontal propagation speed (sections. 3c and 4a and appendix B)
IGW	Internal gravity waves (section 1)
TGE	Taylor–Goldstein equation, used to calculate linear IGW speeds (section 4b and appendixes D and E)
$c_a$	Linear IGW propagation speed in the ambient ahead of the plume (section 4b and appendix D)
$c_u$	Linear IGW propagation speed in the ambient under the plume (section 4b and appendix E)
$c_{nl}$	Nonlinear IGW propagation speed in the ambient under the plume (section 4b and appendix E)
$F_a$	Ambient Froude number ahead of the plume front, i.e., on the saline side (section 4b)
$F_u$	Ambient Froude number under the plume (section 4b)

unchanged in bottom water column) density profile and the velocity profiles per period are shown in Fig. E1.

The nonlinear speed correction  $c' = c_{nl} - c_u$  is linear in the amplitude of the soliton (Ostrovsky and Stepanyants 1989), that is, the vertical isopycnal displacement  $\eta(z)$  of greatest magnitude within the disturbance,  $\eta_0$ . We take  $\eta_0 = 2$  m, an estimate of observed IGW isopycnal displacements (Fig. 6) during late period 1 and period 2. The results of the TGE and KdV calculations per period are given in Table E1 in the form  $a \pm da$ , where  $a$  is the mean value of the particular IGW wave speed at the given period. The value is averaged over the outcomes of different deep stratification profiles as described above, between the 0% and  $\pm 50\%$  cases (trial and error suggests intermediate cases give velocities falling between these). Error ( $\pm$ ) values given are the maximal deviation between the two extreme stratification cases and the average.

## APPENDIX F

### Terms and Acronyms

Terms, acronyms, and symbols used often in the text are listed in Table F1.

### REFERENCES

- Androulidakis, Y. S., V. H. Kourafalou, and R. V. Schiller, 2015: Process studies on the evolution of the Mississippi river plume: Impact of topography, wind and discharge conditions. *Cont. Shelf Res.*, **107**, 33–49, <https://doi.org/10.1016/j.csr.2015.07.014>.
- Benjamin, T. B., 1968: Gravity currents and related phenomena. *J. Fluid Mech.*, **31**, 209–248, <https://doi.org/10.1017/S0022112068000133>.
- Britter, R., and J. Simpson, 1978: Experiments on the dynamics of a gravity current head. *J. Fluid Mech.*, **88**, 223–240, <https://doi.org/10.1017/S0022112078002074>.
- D'Asaro, E. A., and Coauthors, 2018: Ocean convergence and the dispersion of flotsam. *Proc. Natl. Acad. Sci. USA*, **115**, 1162–1167, <https://doi.org/10.1073/pnas.1718453115>.
- Garvine, R. W., and J. D. Monk, 1974: Frontal structure of a river plume. *J. Geophys. Res.*, **79**, 2251–2259, <https://doi.org/10.1029/JC079i015p02251>.
- Gill, A. E., 1982: *Atmosphere—Ocean Dynamics*. Elsevier, 662 pp.
- Goldman, R., M. Ungarish, and I. Yavneh, 2014: Gravity currents with double stratification: A numerical and analytical investigation. *Environ. Fluid Mech.*, **14**, 471–499, <https://doi.org/10.1007/s10652-013-9288-1>.
- Gordon, R. L., 1996: *Acoustic Doppler Current Profiler Principles of Operation: A Practical Primer*. RD Instruments, 57 pp.
- Griffiths, R., 1986: Gravity currents in rotating systems. *Annu. Rev. Fluid Mech.*, **18**, 59–89, <https://doi.org/10.1146/annurev.fl.18.010186.000423>.
- Helfrich, K. R., and W. K. Melville, 2006: Long nonlinear internal waves. *Annu. Rev. Fluid Mech.*, **38**, 395–425, <https://doi.org/10.1146/annurev.fluid.38.050304.092129>.
- Horner-Devine, A. R., 2009: The bulge circulation in the columbia river plume. *Cont. Shelf Res.*, **29**, 234–251, <https://doi.org/10.1016/j.csr.2007.12.012>.
- , D. A. Jay, P. M. Orton, and E. Y. Spahn, 2009: A conceptual model of the strongly tidal columbia river plume. *J. Mar. Syst.*, **78**, 460–475, <https://doi.org/10.1016/j.jmarsys.2008.11.025>.
- , R. D. Hetland, and D. G. MacDonald, 2015: Mixing and transport in coastal river plumes. *Annu. Rev. Fluid Mech.*, **47**, 569–594, <https://doi.org/10.1146/annurev-fluid-010313-141408>.
- Jagannathan, A., K. B. Winters, and L. Armi, 2017: Stability of stratified downslope flows with an overlying stagnant isolating layer. *J. Fluid Mech.*, **810**, 392–411, <https://doi.org/10.1017/jfm.2016.683>.
- Johnson, E. S., 1996: A convergent instability wave front in the central tropical pacific. *Deep-Sea Res. II*, **43**, 753–778, [https://doi.org/10.1016/0967-0645\(96\)00034-3](https://doi.org/10.1016/0967-0645(96)00034-3).

- Kilcher, L. F., and J. D. Nash, 2010: Structure and dynamics of the columbia river tidal plume front. *J. Geophys. Res.*, **115**, C05S90, <https://doi.org/10.1029/2009JC006066>.
- Lee, C.-Y., and R. C. Beardsley, 1974: The generation of long nonlinear internal waves in a weakly stratified shear flow. *J. Geophys. Res.*, **79**, 453–462, <https://doi.org/10.1029/JC079i003p00453>.
- Luketina, D. A., and J. Imberger, 1987: Characteristics of a surface buoyant jet. *J. Geophys. Res.*, **92**, 5435–5447, <https://doi.org/10.1029/JC092iC05p05435>.
- Mahadevan, A., G. S. Jaeger, M. Freilich, M. M. Omand, E. L. Shroyer, and D. Sengupta, 2016: Freshwater in the bay of bengal: Its fate and role in air-sea heat exchange. *Oceanography*, **29**, 72–81, <https://doi.org/10.5670/oceanog.2016.40>.
- Marmorino, G., and C. Trump, 2000: Gravity current structure of the chesapeake bay outflow plume. *J. Geophys. Res.*, **105**, 28 847–28 861, <https://doi.org/10.1029/2000JC000225>.
- Maslowe, S., and L. Redekopp, 1980: Long nonlinear waves in stratified shear flows. *J. Fluid Mech.*, **101**, 321–348, <https://doi.org/10.1017/S0022112080001681>.
- Maxworthy, T., J. Leilich, J. Simpson, and E. Meiburg, 2002: The propagation of a gravity current into a linearly stratified fluid. *J. Fluid Mech.*, **453**, 371–394, <https://doi.org/10.1017/S0022112001007054>.
- McWilliams, J. C., 2016: Submesoscale currents in the ocean. *Proc. Roy. Soc.*, **472A**, 20160117, <https://doi.org/10.1098/rspa.2016.0117>.
- Molinari, R., and A. Kirwan Jr., 1975: Calculations of differential kinematic properties from Lagrangian observations in the western Caribbean sea. *J. Phys. Oceanogr.*, **5**, 483–491, [https://doi.org/10.1175/1520-0485\(1975\)005<0483:CODKPF>2.0.CO;2](https://doi.org/10.1175/1520-0485(1975)005<0483:CODKPF>2.0.CO;2).
- Nash, J. D., and J. N. Moum, 2005: River plumes as a source of large-amplitude internal waves in the coastal ocean. *Nature*, **437**, 400–403, <https://doi.org/10.1038/nature03936>.
- Novelli, G., C. M. Guigand, C. Cousin, E. H. Ryan, N. J. Laxague, H. Dai, B. K. Haus, and T. M. Özgökmen, 2017: A biodegradable surface drifter for ocean sampling on a massive scale. *J. Atmos. Oceanic Technol.*, **34**, 2509–2532, <https://doi.org/10.1175/JTECH-D-17-0055.1>.
- Orton, P. M., and D. A. Jay, 2005: Observations at the tidal plume front of a high-volume river outflow. *Geophys. Res. Lett.*, **32**, L11605, <https://doi.org/10.1029/2005GL022372>.
- Ostrovsky, L., and Y. A. Stepanyants, 1989: Do internal solitons exist in the ocean? *Rev. Geophys.*, **27**, 293–310, <https://doi.org/10.1029/RG027i003p00293>.
- O'Donnell, J., 2010: The dynamics of estuary plumes and fronts. *Contemporary Issues in Estuarine Physics*, Cambridge University Press, 186–246.
- , G. O. Marmorino, and C. L. Trump, 1998: Convergence and downwelling at a river plume front. *J. Phys. Oceanogr.*, **28**, 1481–1495, [https://doi.org/10.1175/1520-0485\(1998\)028<1481:CADAAR>2.0.CO;2](https://doi.org/10.1175/1520-0485(1998)028<1481:CADAAR>2.0.CO;2).
- Pan, J., and D. A. Jay, 2009: Dynamic characteristics and horizontal transports of internal solitons generated at the Columbia River plume front. *Cont. Shelf Res.*, **29**, 252–262, <https://doi.org/10.1016/j.csr.2008.01.002>.
- Pham, H. T., and S. Sarkar, 2018: Ageostrophic secondary circulation at a submesoscale front and the formation of gravity currents. *J. Phys. Oceanogr.*, **48**, 2507–2529, <https://doi.org/10.1175/JPO-D-17-0271.1>.
- Rasche, N., J. Molemaker, L. Marié, F. Nougier, B. Chapron, B. Lund, and A. Mouche, 2017: Intense deformation field at oceanic front inferred from directional sea surface roughness observations. *Geophys. Res. Lett.*, **44**, 5599–5608, <https://doi.org/10.1002/2017GL073473>.
- Rouse, L., 1998: Circulation and hydrographic structure in the vicinity of the Mississippi River Delta. An Observational Study of the Mississippi-Atchafalaya Coastal Plume, S. P. Murray, Ed., Final Rep. OCS Study MMS 98-0040, Minerals Management Service, 107–124.
- Sarkar, S., H. T. Pham, S. Ramachandran, J. D. Nash, A. Tandon, J. Buckley, A. A. Lotliker, and M. M. Omand, 2016: The interplay between submesoscale instabilities and turbulence in the surface layer of the bay of bengal. *Oceanography*, **29**, 146–157, <https://doi.org/10.5670/oceanog.2016.47>.
- Schiller, R., V. Kourafalou, P. Hogan, and N. Walker, 2011: The dynamics of the Mississippi River plume: Impact of topography, wind and offshore forcing on the fate of plume waters. *J. Geophys. Res.*, **116**, C06029, <https://doi.org/10.1029/2010JC006883>.
- Simpson, J. E., 1997: *Gravity Currents: In the Environment and the Laboratory*. Cambridge University Press, 258 pp.
- Ungarish, M., 2006: On gravity currents in a linearly stratified ambient: A generalization of benjamin's steady-state propagation results. *J. Fluid Mech.*, **548**, 49–68, <https://doi.org/10.1017/S0022112005007421>.
- , 2009: *An Introduction to Gravity Currents and Intrusions*. CRC Press, 512 pp.
- , 2012: Gravity currents and intrusions of stratified fluids into a stratified ambient. *Environ. Fluid Mech.*, **12**, 115–132, <https://doi.org/10.1007/s10652-011-9216-1>.
- , and H. E. Huppert, 2002: On gravity currents propagating at the base of a stratified ambient. *J. Fluid Mech.*, **458**, 283–301, <https://doi.org/10.1017/S0022112002007978>.
- , and —, 2006: Energy balances for propagating gravity currents: Homogeneous and stratified ambients. *J. Fluid Mech.*, **565**, 363–380, <https://doi.org/10.1017/S0022112006001455>.
- Walker, N. D., W. J. Wiseman Jr., L. J. Rouse Jr., and A. Babin, 2005: Effects of river discharge, wind stress, and slope eddies on circulation and the satellite-observed structure of the Mississippi River plume. *J. Coastal Res.*, **21**, 1228–1244, <https://doi.org/10.2112/04-0347.1>.
- Warner, S. J., R. M. Holmes, E. H. M. Hawkins, M. S. Hoecker-Martínez, A. C. Savage, and J. N. Moum, 2018: Buoyant gravity currents released from tropical instability waves. *J. Phys. Oceanogr.*, **48**, 361–382, <https://doi.org/10.1175/JPO-D-17-0144.1>.
- White, B. L., and K. R. Helfrich, 2008: Gravity currents and internal waves in a stratified fluid. *J. Fluid Mech.*, **616**, 327–356, <https://doi.org/10.1017/S0022112008003984>.
- , and —, 2012: A general description of a gravity current front propagating in a two-layer stratified fluid. *J. Fluid Mech.*, **711**, 545–575, <https://doi.org/10.1017/jfm.2012.409>.
- Wright, L., and J. M. Coleman, 1971: Effluent expansion and interfacial mixing in the presence of a salt wedge, Mississippi River Delta. *J. Geophys. Res.*, **76**, 8649–8661, <https://doi.org/10.1029/JC076i036p08649>.
- Yankovsky, A. E., and D. C. Chapman, 1997: A simple theory for the fate of buoyant coastal discharges. *J. Phys. Oceanogr.*, **27**, 1386–1401, [https://doi.org/10.1175/1520-0485\(1997\)027<1386:ASTFTF>2.0.CO;2](https://doi.org/10.1175/1520-0485(1997)027<1386:ASTFTF>2.0.CO;2).